PCCP

PAPER

View Article Online
View Journal | View Issue

Cite this: *Phys. Chem. Chem. Phys.*, 2026, **28**, 1148

Coexistence of ferromagnetism and enhanced photo-response in Fe-doped $SnSe_2$ single crystals

Aarti Lakhara and P. A. Bhobe *

In this work, we report the synthesis and comprehensive characterization of pristine and Fe-doped $SnSe_2$ single crystals, revealing how light Fe doping enhances photoconductivity and induces magnetism in this layered 2D material. Fe substitution leads to a reduction in its band-gap and activation energy, as noted from its electrical transport measurements. Its phonon characteristics and crystal symmetry remain unaltered, as confirmed from temperature-dependent Raman spectroscopy measurements. Magnetic measurements demonstrate that even low Fe concentrations induce a ferromagnetic interaction in otherwise diamagnetic pristine $SnSe_2$ and this interaction increases with increasing Fe-concentration. Photoconductivity measurements demonstrate a pronounced superlinear photocurrent response in both pristine and Fe-doped $SnSe_2$-based photodetectors. A model based on three recombination centers is proposed to explain this superlinear behavior. Interestingly, 1% Fe-doped $SnSe_2$ exhibits the highest external quantum efficiency ($\sim 1.4 \times 10^4$%) and detectivity ($\sim 10^{12}$ Jones), along with a reduced response time. The coexistence of robust ferromagnetism and superior photodetector performance in Fe-doped $SnSe_2$ highlights its potential as a promising candidate for next-generation spintronic, optoelectronic, and energy-related applications.

Received 8th September 2025,
Accepted 6th December 2025

DOI: 10.1039/d5cp03461b

rsc.li/pccp

1 Introduction

Two-dimensional (2D) transition metal dichalcogenides beyond graphene have garnered significant attention due to their suitable band gap range,[1] making them promising candidates for a variety of electronic and optoelectronic applications.[2] These materials exhibit a wide range of crystal structures, enabling the emergence of diverse electronic phases, including semiconducting, metallic, and even superconducting states.[3] Their layered architecture further allows for fine-tuning of intrinsic properties through external modifications.[4,5]

A representative material, $SnSe_2$, stands out for its high carrier mobility[6,7] and strong photoresponse,[8,9] with ultrathin devices achieving responsivity $>10^3$ A W^{-1} and response times <15 ms.[10] Flexible, broadband $SnSe_2$ photodetectors have further enhanced its potential for wearable electronic applications.[11] Although advancements have been made in terms of nanoelectronics-relevant properties of $SnSe_2$, the impact of magnetic transition metal doping on its structural, optical, electrical, and magnetic behavior remains largely unexplored. Existing studies have mostly focused on its magnetic aspects. For instance, Mn-doped $SnSe_2$ thin films have been studied for their room-temperature ferromagnetism,[12] while their single-crystalline counterparts show spin-glass-like behavior below 60 K.[13] However, the corresponding vibrational and transport properties have not been systematically investigated. Similarly, vanadium (V) doping in $SnSe_2$ has not been studied beyond its structural aspects.[14]

In this study, we aim to investigate the influence of Fe doping in $SnSe_2$ on its electrical, vibrational, magnetic, and photoconductive properties, with the goal of understanding the resulting modifications in its structural and functional behavior. Incorporating Fe can increase the valence band maximum and decrease the conduction band minimum; hence, a change in the Fermi energy makes it suitable for photodetector applications.[15–18] We prepared pristine and Fe-doped $SnSe_2$ bulk single crystals using the chemical vapor transport method. The properties of well-characterized samples were examined and it was found that even a small doping concentration of Fe ($\sim$1%) can significantly impact the intrinsic properties of $SnSe_2$. This will be discussed through temperature-dependent transport and magnetic measurements, temperature-dependent Raman studies and room temperature photo-conductivity measurements. The analysis of photoconductivity properties shows giant superlinearity in $SnSe_2$ and Fe-doped $SnSe_2$ single crystal based photodetectors. The Fe-doping reduces the band gap which results in a faster photoresponse.

The dual enhancement of magnetic and photoconductive functionalities highlights the efficacy of transition metal doping as a tunable strategy for engineering the electronic, magnetic, and optoelectronic properties of layered 2D materials.

Department of Physics, Indian Institute of Technology Indore, Khandwa Road, Indore, Simrol 453552, India. E-mail: pbhobe@iiti.ac.in

The observed coexistence of magnetic ordering and high-performance photodetection within a single crystalline platform not only provides insights into dopant-induced interactions in $SnSe_2$, but also paves the way for multifunctional device architectures, such as magnetic photodetectors and integrated photodetector–spin valve systems. These results underscore the potential of Fe-doped $SnSe_2$ as a versatile material candidate for next-generation spintronic, optoelectronic, and energy-related applications.

2 Experimental

Single crystals of $SnSe_2$ were synthesized using the chemical vapor transport (CVT) method. High-purity Sn and Se elements (Alfa Aesar, >99.99%) were mixed in a 1 : 2 molar ratio, sealed in an evacuated quartz tube under a pressure of 10^{-5} mbar, and placed in a CVT furnace. A temperature gradient from 660 °C (source zone) to 500 °C (growth zone) was maintained for three days, followed by slow cooling to room temperature. Millimeter-sized single crystalline flakes of $SnSe_2$ were collected from the cold end of the tube. Fe-doped $SnSe_2$ single crystals with 1% and 3% Fe contents were prepared using a two-step process. Initially, polycrystalline precursors were synthesized by heating stoichiometric mixtures of Fe, Sn, and Se at 600 °C for two days. The resulting powders were sealed in a quartz tube and subjected to the same CVT protocol as used for pristine $SnSe_2$ crystal growth. Elemental composition and uniformity of Fe, Sn, and Se distribution were verified by energy dispersive spectroscopy (EDS). The crystal structure and phase purity were confirmed by X-ray diffraction (XRD), while the quality of the as-grown crystals was further evaluated using Raman spectroscopy (LabRAM HR Evolution, Horiba Scientific). Temperature-dependent Raman spectra were recorded using a liquid nitrogen cooled charge coupled device detector with a Linkam stage. The magnetization measurement was performed using a Quantum Design MPMS3 Squid magnetometer.

Electrical resistivity measurements were performed using a two-probe method on single crystalline flakes with dimensions of ∼1 mm length and micrometer-scale thickness. Conductive silver paste was used to form electrical contacts. Measurements were conducted in the 20–300 K temperature range using a helium-based closed-cycle refrigerator (CCR) controlled by a Lakeshore 335 temperature controller. A Keithley 6512B electrometer was used for current measurement, with data acquisition handled *via* a LABVIEW 8.5 interface. The photoconductivity measurements were carried out using a Keithley 6517B electrometer in conjunction with a Kessil PR160L-440 nm light source with variable power output features.

3 Results and discussion

$SnSe_2$ is a van der Waals (vdW) layered material with a hexagonal crystal structure (space group $P\bar{3}m1$), as illustrated in Fig. 1(a). Each layer consists of a Sn atomic plane sandwiched between two Se atomic planes, forming a Se–Sn–Se layer. In this structure, both Sn and doped Fe atoms are coordinated with six Se atoms, forming $(Sn,Fe)Se_6$ octahedra. The elemental composition and even distribution of each element in the prepared crystals were confirmed by elemental mapping using EDS

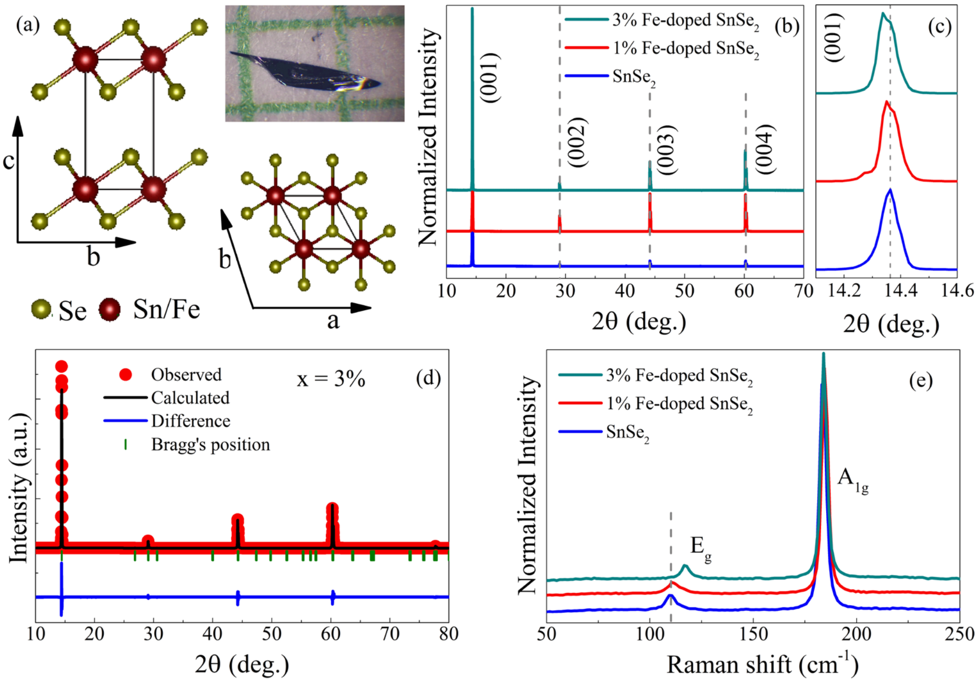

Fig. 1 (a) The schematic shows the crystal structure of $(Sn,Fe)Se_2$ along different directions, along with an optical microscopy image of an Fe-doped $SnSe_2$ single crystal; scale bar is 1 mm. (b) X-ray diffraction (XRD) pattern of $Sn_{1-x}Fe_xSe_2$ with x = 0%, 1%, and 3%, respectively. (c) Zoomed-in view of the (001) diffraction peak of all the compositions. (d) Le-Bail refined XRD pattern of 3% Fe-doped $SnSe_2$. (e) Room temperature Raman spectra of all the samples; dashed line is guide to the eye to show the shift.

spectra as shown in Fig. S1. The exact atomic % of each element in the synthesized crystal is also tabulated in Section S1. It should be noted that in 1% Fe-doped $SnSe_2$, Fe is 2.6% of the Sn content, while in 3% Fe-doped $SnSe_2$, Fe is 7.3% of the Sn content. The crystal structures of all the synthesized crystals were examined by X-ray diffraction (XRD). Fig. 1(b) shows the XRD patterns recorded from the respective single-crystalline flakes. Due to the low concentration of Fe doping, the overall crystal structure of $(Sn,Fe)Se_2$ remains nearly identical to that of pristine $SnSe_2$, with no detectable secondary phases. The sharp diffraction peaks observed in all three compositions reflect the highly oriented nature and excellent crystallinity of the single crystals. As shown in Fig. 1(c), close inspection of the X-ray diffraction peak reveals a peak shift towards a lower angle, providing a hint that a few Fe-atoms might be introduced between the layer spacing. Additionally, with Fe-doping, the full width at half-maximum (FWHM) of the diffraction peak increases, confirming the effective incorporation of Fe into the lattice. Le Bail refinement was carried out using the FullProf suite[19,20] and the refined structure of 3% Fe-doped $SnSe_2$ is shown in Fig. 1(c). The refined lattice parameters for both pristine and Fe-doped $SnSe_2$ remain consistent within the margin of experimental error, yielding values of $a = b = 3.85$ Å and $c = 6.14$ Å. The absence of any significant change in lattice constants confirms that Fe doping does not disrupt the long-range crystal structure. This structural stability makes Fe-doped $SnSe_2$ an ideal platform to investigate the impact of doping on its magnetic and electronic-transport properties.

Raman spectroscopy, a powerful tool for probing lattice vibrations and phase transitions in two-dimensional materials, was employed to assess the structural integrity and lattice dynamics of Fe-doped $SnSe_2$ single crystals. Room-temperature Raman measurements were conducted using a 633 nm laser excitation to evaluate the quality of the synthesized crystals. As shown in Fig. 1(e), both pristine and Fe-doped $SnSe_2$ samples exhibited two prominent Raman active modes corresponding to the in-plane (E_g) and out-of-plane (A_{1g}) vibrations, consistent with group theory predictions and previous reports.[21,22] Importantly, no additional peaks were observed in the Fe-doped samples compared to the pristine $SnSe_2$, indicating that Fe incorporation does not introduce any secondary phase or alter the intrinsic lattice vibrational modes. This suggests that the crystallographic symmetry of the host material is preserved upon doping. However, a noticeable blue shift in the Raman modes was detected in the Fe-doped samples, which is in line with a slight reduction in the lattice constant observed from XRD analysis. This effect can be related to the substitution of the Sn atom (Sn^{4+} = 0.69 Å) with a smaller sized Fe (Fe^{3+} = 0.55 Å; Fe^{2+} = 0.61 Å) atom. This spectral shift provides compelling evidence that Fe atoms are successfully integrated into the $SnSe_2$ lattice without disrupting its fundamental structural framework.

3.1 Vibrational properties

To gain deeper insight into phonon decay processes and the effect of Fe-doping on the lattice dynamics, we conducted temperature-dependent Raman measurements. As the temperature increases, both Raman modes exhibit a red-shift. Despite the introduction of Fe, the overall temperature-dependent lattice dynamics remain consistent across different doping levels. Consequently, representative Raman spectra for the 3% Fe-doped $SnSe_2$ sample are presented in Fig. 2(a). It is evident that temperature significantly affects the Raman peak positions. In the case of 3% Fe-doped $SnSe_2$, the most intense A_{1g} mode at 188.7 cm^{-1} shifts by 5.51 cm^{-1} as the temperature increases from 93 K to 423 K. For temperatures above 193 K, the Raman mode peak position exhibits a linear dependence on temperature, which can be described by a first-order temperature coefficient (χ) according to the equation $\omega(T) = \omega_0 + \chi T$, where ω_0 represents the phonon frequency at 0 K. The extracted first-order temperature coefficients for all compositions are summarized in Table 1. These values show good agreement with previously reported data for both single crystals and nanosheets.[23,24]

It is observed that Fe doping alters the system's sensitivity to temperature change, likely due to the introduction of extra charge carriers, which modulate the thermal properties. The anharmonic contributions to the phonon behavior, as proposed by Balkanski *et al.*,[25] are modeled using the expression

$$\omega(T) = \omega_0 + A\left[1 + \frac{2}{\exp(x) - 1}\right] + B\left[1 + \frac{3}{\exp(y) - 1} + \frac{3}{(\exp(y) - 1)^2}\right],$$

where $x = \hbar\omega_0/2k_BT$, $y = \hbar\omega_0/3k_BT$, ω_0 is the phonon frequency at $T = 0$ K, $\hbar$ is the reduced Planck's constant, k_B is the Boltzmann constant, and A and B are anharmonic constants. The fitting parameters, including the anharmonic constants A and B, are summarized in Table 1.

For all analyzed Raman modes of $SnSe_2$ and Fe-doped $SnSe_2$, the anharmonic constant A is consistently several times larger than B for each composition. This suggests that three-phonon decay processes or intrinsic anharmonicity dominate the phonon dynamics, even after Fe doping. It also indicates that Fe-doping is not entirely disruptive of the electronic structure of $SnSe_2$. However, the relative variation of the anharmonic constants across compositions, say for the E_g mode, shows a more pronounced change in the B coefficient compared to A. This points to the influence of Fe doping on introducing additional charge carriers, which in turn affects both anharmonicity and electron–phonon interactions.

3.2 Magnetic properties

The temperature-dependent magnetization measurement (M *vs.* T) of $SnSe_2$ and Fe-doped $SnSe_2$ under an applied magnetic field of 1 T is shown in Fig. 3(a). It is evident from Fig. 3(a) that $SnSe_2$ shows diamagnetic behavior from room temperature down to $T \approx 8$ K, consistent with previous studies.[13] Below 8 K, a transition from diamagnetic to paramagnetic behavior can be seen. With an increase in Fe concentration, this

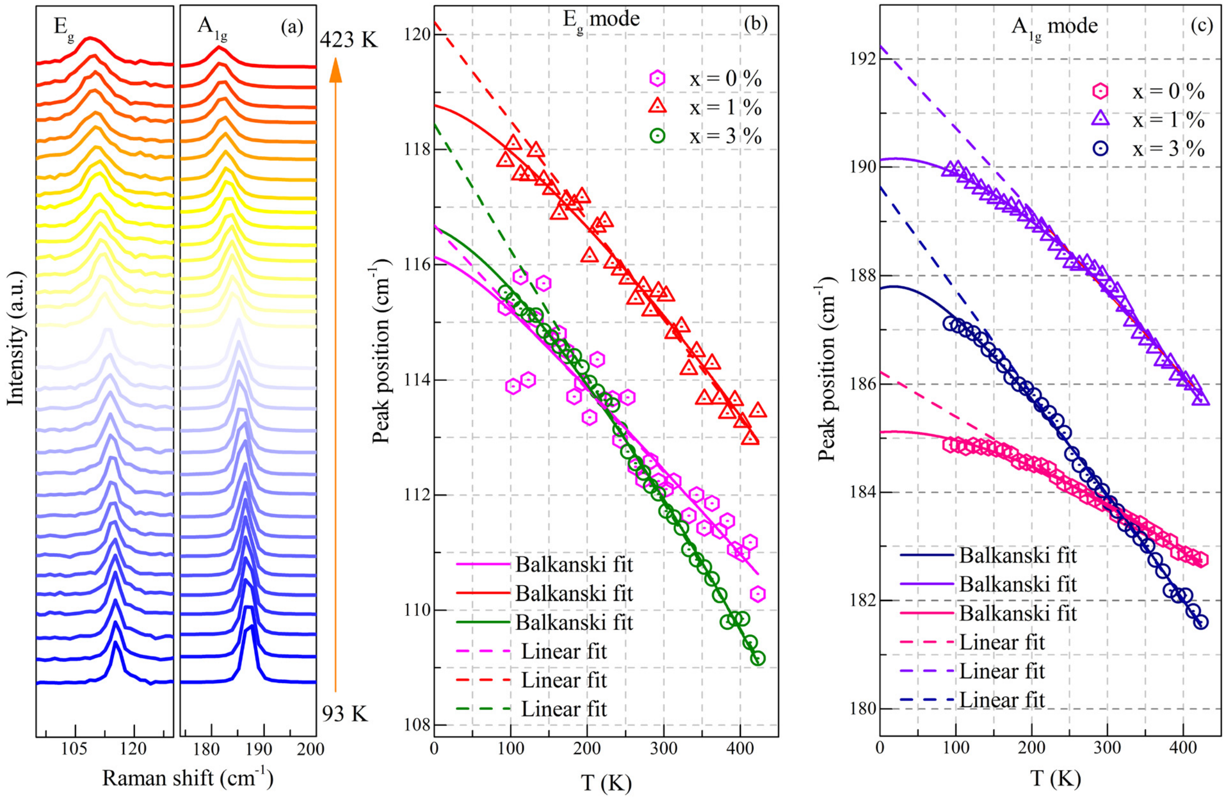

Fig. 2 (a) Temperature-dependent Raman spectra of 3% Fe-doped $SnSe_2$ from 93 K to 423 K. Temperature-dependent Raman shift of the (b) E_g mode and (c) A_{1g} mode for all the compositions, where solid lines represent Balakanski fit and dashed lines represent linear fit.

Table 1 Calculated parameters from Balkanski fit and first order temperature coefficient for $SnSe_2$ and Fe-doped $SnSe_2$

	$SnSe_2$		1% Fe-doped $SnSe_2$		3% Fe-doped $SnSe_2$	
	E_g	A_{1g}	E_g	A_{1g}	E_g	A_{1g}
ω_0 (cm^{-1})	116.7250	185.4268	119.6882	190.6099	117.14407	188.77477
A (cm^{-1})	−0.7914	−0.2077	−0.81025	−0.2896	−0.73859	−1.02067
B (cm^{-1})	−0.00818	−0.1108	−0.02409	−0.23662	−0.06772	−0.17171
χ (cm^{-1})	−0.01425	−0.0081	−0.01627	−0.01471	−0.02147	−0.01907

transition from diamagnetic behavior to paramagnetic behavior shifts towards higher temperatures. This transition temperature is 114 K and 140 K for 1% Fe-doped and 3% Fe-doped compositions, respectively. To understand these diamagnetic and paramagnetic contributions, we attempted to fit M/H (dc-magnetic susceptibility (χ_{dc})) using the expression[26]

$$\chi = \chi_0 + D \times T + C/(T + \theta)$$

Here the first two terms describe the diamagnetic contribution and the third term represents the Curie–Weiss law, which describes the paramagnetic contribution. C is the Curie–Weiss constant and θ is the magnetic ordering temperature. As shown in Fig. 3(c) and (d), experimental data fit well with this equation, confirming both the contributions. The values of Curie–Weiss constant C obtained from the fitting are 5.4×10^{-6} emu K per g Oe and 30.4×10^{-6} emu K per g Oe for 1% Fe-doped $SnSe_2$ and 3% Fe-doped $SnSe_2$, respectively. The effective magnetic moments, as inferred from the Curie constant values, are $4.3\mu_B$ for 1% Fe-doped $SnSe_2$ and $21.3\mu_B$ for 3% Fe-doped $SnSe_2$. For 1% Fe-doped $SnSe_2$, the obtained effective moment value ($4.3\mu_B$) is close to the effective magnetic moment value ($4.9\mu_B$) for Fe^{2+} ($3d^6$) in a high spin configuration (t_{2g}^4 e_g^2), which is commonly observed in dichalcogenides.[27] The presence of a weak-field ligand (Se^{2-}) results in a low crystal field splitting energy, favoring the high-spin Fe^{2+} state, whereas a very high effective magnetic moment obtained for 3% Fe-doped $SnSe_2$ ($21.3\mu_B$) suggests the presence of the +3 oxidation state of Fe in addition to the +2 state in this composition and also that magnetic interactions play an important role, which needs further investigation. As the Fe doping level increases from 1% to 3%, the Fe/Se ratio changes, modifying the local

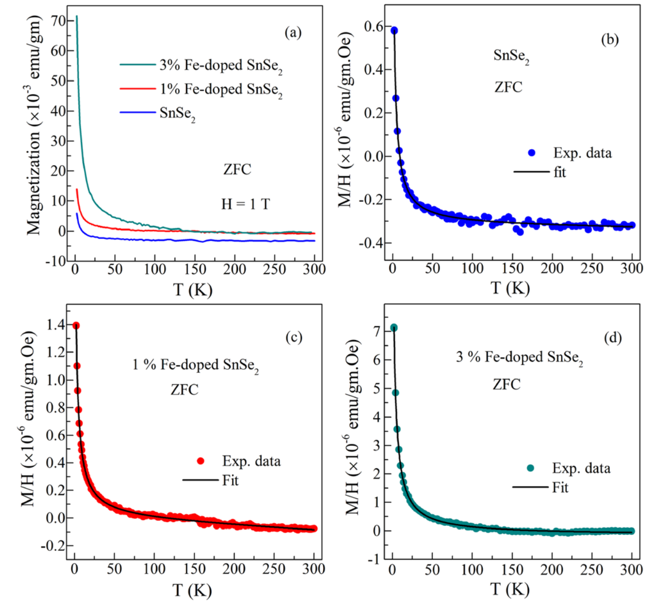

Fig. 3 (a) Temperature-dependent magnetization of 3% Fe-doped $SnSe_2$, 1% Fe-doped $SnSe_2$ and $SnSe_2$ at an applied magnetic field H = 1 T with a zero field cooling protocol. (b)–(d) Temperature-dependent M/H for each composition and the black line shows fitting the magnetic susceptibility expression as given in the main text.

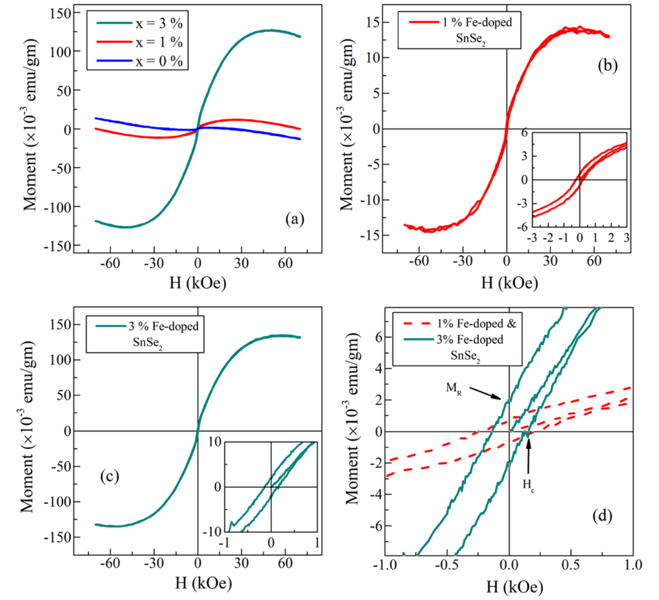

Fig. 4 (a) Magnetic field-dependent magnetization (M–H curve) for all the compositions at T = 5 K. (b) M–H curve for 1% Fe-doped $SnSe_2$ after subtracting the diamagnetic contribution of $SnSe_2$ and (c) M–H curve for 3% Fe-doped $SnSe_2$ after subtracting the diamagnetic contribution of $SnSe_2$. (d) A comparison of the M–H curve of 1% Fe-doped and 3% Fe-doped $SnSe_2$.

crystal field environment and potentially stabilizing a larger proportion of Fe^{3+} species.[28] Therefore, based on the magnetic moment analysis and structural considerations, Fe likely exists in a mixed-valence state (Fe^{2+}/Fe^{3+}) in both 1% and 3% Fe-doped $SnSe_2$, with the relative dominance of each oxidation state depending on the Fe concentration.

To further investigate the influence of Fe concentration on the magnetic properties of $SnSe_2$, field-dependent magnetization (M–H) measurements were conducted at T = 5 K for all samples, as illustrated in Fig. 4(a). The pristine $SnSe_2$ sample exhibits diamagnetic behavior and upon doping with 1% Fe and 3% Fe, ferromagnetic interactions emerge, as evidenced in Fig. 4(b) and (c). The diamagnetic contribution of $SnSe_2$ was subtracted from the doped compositions, revealing a clearer ferromagnetic signature. The zoomed-in view of low magnetic fields is shown in the inset of Fig. 4(b), which displays a distinct hysteresis loop, confirming the presence of ferromagnetic interactions. The magnetic moment increases significantly from 1% Fe to 3% Fe as shown in Fig. 4(c), along with hysteresis at low magnetic fields (inset of Fig. 4(c)). To examine the evolution of hysteresis behavior at low magnetic fields with varying Fe concentrations, M–H curves for 1% and 3% Fe-doped $SnSe_2$ are plotted together, as shown in Fig. 4(d). From these curves, the coercivity (H_C) and remnant magnetization (M_R) values were extracted. The coercivity decreases from 230 Oe to 129 Oe with increasing Fe concentration, while the remnant magnetization increases from 0.72×10^{-3} emu g^{-1} to 2.02×10^{-3} emu g^{-1}. Overall, the magnetic measurements suggest that the 3% Fe-doped $SnSe_2$ sample exhibits characteristics of a soft ferromagnet, with enhanced magnetic ordering and improved ease of magnetization and demagnetization.

3.3 Electrical transport

The temperature-dependent electrical resistance of pristine $SnSe_2$ single crystals is shown in Fig. 5(a). The material exhibits semiconducting behavior across the entire temperature range of 20 K to 300 K, with the resistance decreasing as the temperature increases. This semiconducting nature of the sample is consistent with previous reports.[29] In the intermediate temperature range, the data fit well to the thermally activated transport model, described by the equation $R(T) = R_0 \exp(E_a/k_BT)$, where R_0 is a pre-exponential factor, E_a is the thermal activation energy (band gap), and k_B is the Boltzmann constant. As shown in the inset of Fig. 5(a), a linear relationship between $\ln R$ and $1/T$ is observed from 48 K to 95 K, yielding an activation energy of $\sim$5.48 meV. With Fe substitution, the $SnSe_2$ system retains its semiconducting nature, as shown in Fig. 5(b) and (c). However, a reduction in resistance is observed upon doping, consistent with the theoretical prediction that Fe incorporation raises the valence band maximum and lowers the conduction band minimum.[15] The extracted activation energy decreases from 4.71 meV (in 1% Fe) to 3.23 meV (in 3% Fe), indicating band gap narrowing with increasing Fe concentration.

3.4 Photoconductivity properties

To evaluate the photoconductivity properties of pristine and Fe-doped $SnSe_2$ single crystals, photodetectors were fabricated using these crystals and tested under illumination with a 440 nm light source. A schematic diagram of the single-crystal-based photodetector under illumination is shown in

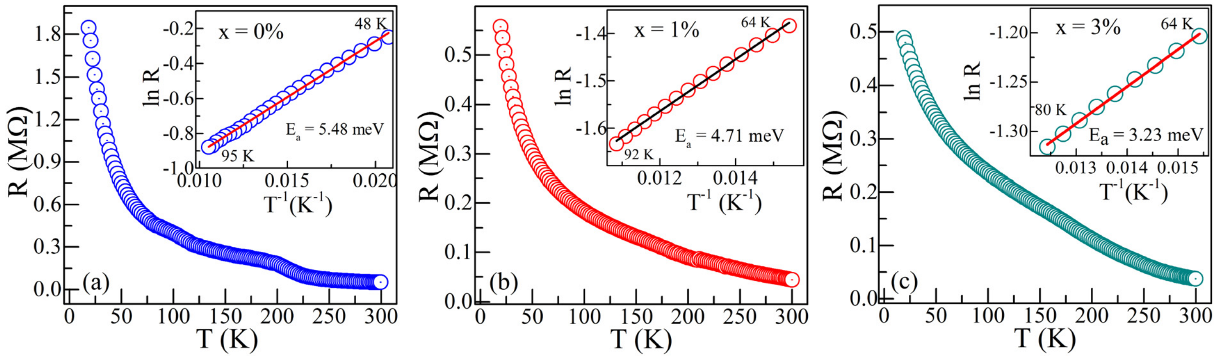

Fig. 5 Temperature-dependent resistance of $Sn_{1-x}Fe_xSe_2$ with x = 0% (a), 1% (b), and 3% (c), respectively.

the inset of Fig. 6(a). As the sample resistance varied with different light intensities, the photocurrent responded accordingly. Fig. 6(a)–(c) show that photodetectors based on both pristine and Fe-doped $SnSe_2$ exhibit linear current–voltage (I–V) characteristics, confirming the formation of stable ohmic contacts. These contacts remained ohmic even under illumination and after Fe doping. However, both light intensity and Fe doping significantly influenced the photodetector's light and dark current levels. The dark current of the Fe-doped $SnSe_2$ device was observed to be higher than that of its pristine counterpart. This increase in dark current is consistent with temperature-dependent transport measurements, which show a reduction in activation energy upon Fe doping. It is also consistent with the analysis of temperature-dependent Raman spectra, which show increased anharmonicity through Balkanski model fitting for Fe doping. The introduction of Fe introduces donor levels just below the conduction band, enabling additional charge carriers to participate in conduction[13,30] as well as in introducing anharmonicity and electron–phonon interactions. A slight decrease in dark current observed at 3% Fe doping may be attributed to increased disorder and carrier scattering as the Fe concentration rises.

The dependence of photocurrent on light intensity for the photodetectors is presented in Fig. 6(d)–(f). The experimental data were fitted using the power-law relation,[31] $I_{ph} = AP^{\gamma}$, where I_{ph} ($=I_{light} - I_{dark}$) defines the photocurrent, P is the incident light intensity, and A is a proportionality constant. The exponent γ characterizes the efficiency of photoinduced charge carrier generation and collection. In an ideal, trap-free photodetector, γ = 1, indicating a linear relationship between photocurrent and light intensity. A value of $\gamma < 1$ implies sublinear behavior, typically attributed to trap states and recombination

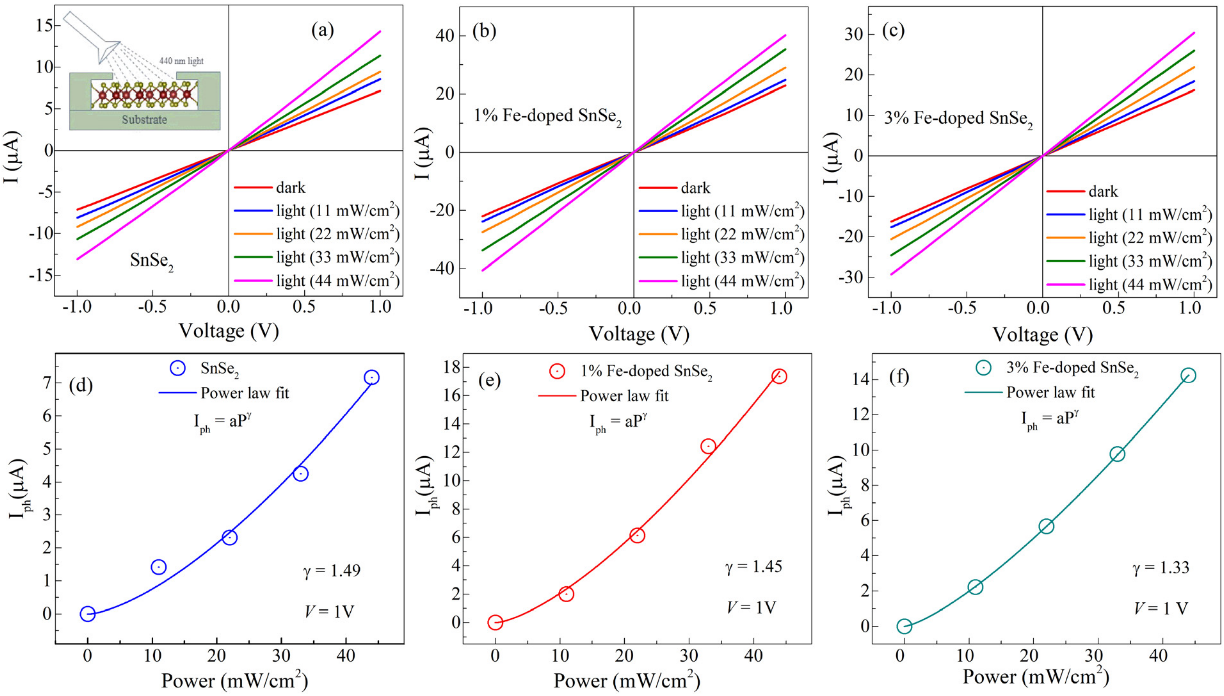

Fig. 6 The current–voltage (I–V) characteristic of the device based on $Sn_{1-x}Fe_xSe_2$ with x = 0% (a), 1% (b), and 3% (c), with a blue 440 nm light with different light intensities respectively. (d)–(f) Power-dependent photo-current for each composition.

processes associated with material defects. Conversely, $\gamma > 1$ reflects superlinear behavior, which can result from thermal effects (*e.g.*, enhanced carrier mobility or reduced recombination) and nonlinear optical phenomena such as carrier multiplication or two-photon absorption. These mechanisms cause the photocurrent to increase faster than linearly with light intensity. As shown in the figure, both pristine and Fe-doped $SnSe_2$ exhibit superlinear responses, with γ values ranging from 1.33 to 1.49. This pronounced superlinearity indicates enhanced optoelectronic performance and is particularly noteworthy given the two-dimensional nature of the materials, where intrinsic defects typically promote recombination and suppress superlinear behavior.[32,33] The underlying mechanisms responsible for this unusually strong superlinearity in $SnSe_2$-based photodetectors will be discussed later in the text. For now, it is sufficient to know that recombination centers (RCs) may arise from in-gap states associated with selenium vacancies or other structural defects[34] and may play a crucial role in the performance of the proposed Fe-doped $SnSe_2$ photodetector.

The performance of a photodetector is commonly evaluated using responsivity (R), a key parameter that quantifies the photocurrent generated per unit of incident light power. Responsivity is defined by the equation $R = \frac{I_{\mathrm{ph}}}{A \cdot P}$, where I_{ph} is the photocurrent, A is the effective illuminated area of the device, and P is the incident light intensity. As shown in Fig. 7(a), the responsivity of both pristine and Fe-doped $SnSe_2$ photodetectors increases with increasing light intensity. This trend suggests that photogeneration is not significantly limited by carrier recombination processes. The enhanced responsivity observed in Fe-doped $SnSe_2$ devices indicates that Fe doping improves photoabsorption—possibly by introducing mid-gap states or reducing the band gap, as supported by our electronic transport measurements, thereby enhancing the material's light-harvesting efficiency.

In addition, two other key parameters used to evaluate photodetector performance are external quantum efficiency (EQE) and detectivity (D). External quantum efficiency quantifies the effectiveness of converting incident photons into charge carriers and is given by the relation $R \times \frac{h\nu}{q}$, where R is the responsivity, h is the Planck constant, ν is the incident light frequency and q is the electron charge. As shown in Fig. 7(b), the 1% Fe-doped $SnSe_2$ device exhibits the highest EQE, comparable to that of other high-performance 2D-material based photodetectors.[35,36] The other important parameter, detectivity (D), defines the device's ability to distinguish weak signals from background noise. It is defined as $R \times \sqrt{\frac{A}{2qI_{\mathrm{dark}}}}$, where, as defined earlier, A is the effective area of the device and I_{dark} is the dark current. As shown in Fig. 7, the photodetectors in this study demonstrate excellent detectivity, reaching values on the order of 10^{12} Jones.

The superior photodetector performance observed at low Fe doping (1%) can be attributed to the optimal introduction of donor-like defect states near the conduction band, which enhance carrier generation and reduce activation energy, as confirmed by temperature-dependent resistance measurements. These defect states facilitate efficient charge transport and light absorption, leading to significantly improved external quantum efficiency (EQE) and detectivity. In contrast, higher Fe concentrations (*e.g.*, 3%) introduce Fe^{3+} character and hence a higher magnetic moment that may lead to a localization of charge carriers, which hinders carrier mobility and reduces photodetector performance. Consequently, a slight reduction in EQE and responsivity is observed for 3% Fe-doped $SnSe_2$, accompanied by an enhanced magnetic moment. Therefore, maintaining a low Fe doping level (1%) yields higher EQE and responsivity along with a moderate magnetic moment, while higher Fe doping (3%) results in reduced photodetector efficiency but enhanced magnetic response, making it suitable for multifunctional device applications.

To investigate the effect of Fe doping on the photoresponse behavior, time-dependent photocurrent measurements were performed. The photocurrent was recorded under a constant bias voltage of 1 V, while the 440 nm laser source was periodically switched on and off to capture the rise and decay dynamics. The photoresponse of pristine and Fe-doped $SnSe_2$ photodetectors at an illumination intensity of 33 mW cm^{-2} is

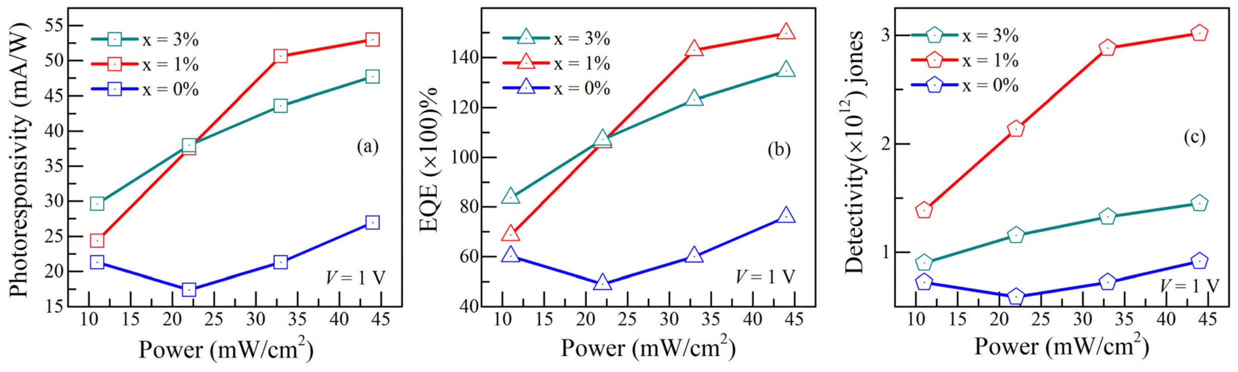

Fig. 7 (a) Photoresponsivity, (b) external quantum efficiency (EQE) and (c) detectivity as a function of power density for $Sn_{1-x}Fe_xSe_2$ with x = 0%, 1%, and 3%, respectively.

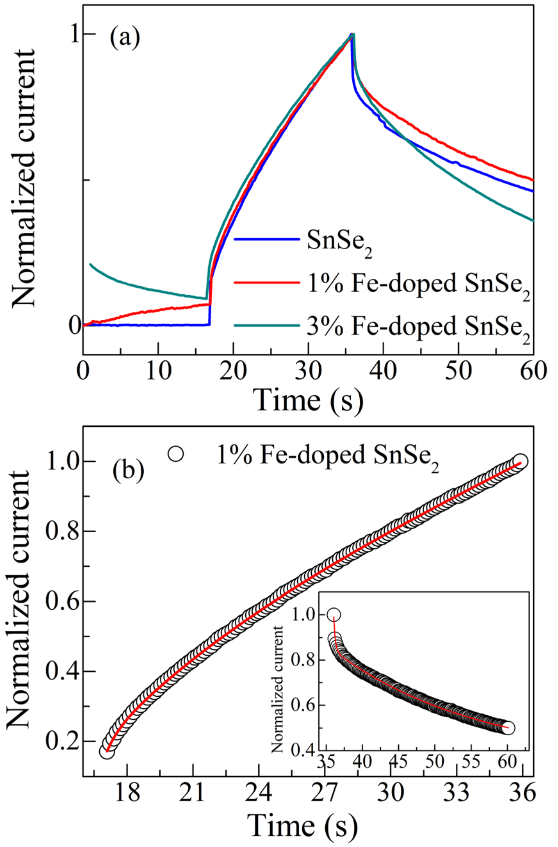

Fig. 8 (a) Comparison of time dependent response of $Sn_{1-x}Fe_xSe_2$ with x = 0%, 1%, and 3%, respectively. (b) Time response of photocurrent growth and decay (inset) for x = 1%; the empty circles are experimental points and the solid lines are fits to exponential equations (see the main text for details).

shown in Fig. 8(a). The rise and decay segments of the photocurrent were fitted using a multi-exponential function,[37,38] defined as $I_{\text{rise}} = I_0 + A_1 e^{x/t_1} + A_2 e^{x/t_2} + A_3 e^{x/t_3}$ and $I_{\text{decay}} = I_0 + A_1 e^{-x/t_1} + A_2 e^{-x/t_2} + A_3 e^{-x/t_3}$, where I_0 is the steady state photocurrent, A_i are fitting constants, and t_i (i = 1, 2, and 3) represent the time constants associated with various carrier relaxation processes. An example of the fitting for the 1% Fe-doped $SnSe_2$ device is shown in Fig. 8(b). The extracted time constants for both rise and decay processes are 728, 500, and 193 ms and 121, 608, and 175 ms for $SnSe_2$, 1% Fe-doped $SnSe_2$ and 3% Fe-doped $SnSe_2$ respectively. All devices exhibit fast photoresponse behavior, with rise and decay times approximately an order of magnitude slower than those of their monolayer counterparts, likely due to the size and thickness effects in the bulk-like crystals. Interestingly, the rise time decreases with increasing Fe concentration, while the decay time increases upon Fe doping. Among all compositions, the 3% Fe-doped $SnSe_2$ photodetector shows the fastest rise time, indicating improved carrier generation dynamics possibly due to enhanced absorption or carrier injection efficiency (Table 2).

The photoresponse (PR) time of a photodetector is governed by two primary processes,[42] electron–hole recombination and carrier transition dynamics. The response time is given by the following relationship:

$$\frac{1}{t_{\text{PR}}} = \frac{1}{t_{\text{rec}}} + \frac{1}{t_t}$$

where t_{rec} is the recombination time and t_t is the carrier transition time. The carrier transition time depends on the mobility of the charge carrier and the thickness of the material channel, both of which may be slightly varied by Fe doping. However, since these changes are relatively minor, the overall response time is primarily dictated by the recombination time. The recombination process itself involves three key stages: (a) hole trapping and de-trapping at recombination center 1 (see Fig. 9), (b) a similar process at recombination center 2, and (c) recombination of excess electrons with holes. Under illumination, electron–hole pairs are generated, and many holes become trapped at recombination centers 1 and 2. These trapped holes are later detrapped back into the valence band, where they can recombine with free electrons. Consequently, the recombination time is primarily determined by the detrapping time, which is given by $1/\tau = SN\nu e^{-\Delta E/kT}$, where S is the capture cross-section of the recombination center, N is the density of states of electrons in the conduction band, ν is the thermal velocity of the carriers, and ΔE is the energy depth of the recombination center to the valence band. A larger ΔE results in a longer detrapping time, thereby slowing the recombination process. Upon Fe doping, the band gap narrows (see Fig. S2 and S3), as confirmed by transport measurements. This reduction in band gap lowers ΔE, leading to shorter detrapping times and thereby faster photoresponse in Fe-doped $SnSe_2$ compared to the pristine material.

We now return to the discussion of the observed superlinear photoresponse behavior in $SnSe_2$ and Fe-doped $SnSe_2$ photodetectors. To explain this phenomenon, we adopt a model based on the trap-assisted recombination mechanism,

Table 2 Photodetector performance in this work compared with other 2D materials

Device	τ (ms)	R (mA W^{-1})	EQE (%)	D (Jones)	Ref.
$SnSe_2$	728	26.92	7.6×10^3	0.91×10^{12}	This work
1% Fe-doped $SnSe_2$	500	53.61	1.4×10^4	3.01×10^{12}	This work
3% Fe-doped $SnSe_2$	193	47.69	1.3×10^4	1.44×10^{12}	This work
Few-layer $SnSe_2$	14.5	1.1×10^6	2.6×10^5	1×10^{10}	10
GaS nanosheets	30	4200	2×10^3	10×10^{12}	36
WSe_2	850	4.48	8	0.32×10^9	39
In-doped SnS_2 nanosheets	13	1.5×10^5	4.7×10^4	5.81×10^{12}	40
Sb-doped SnS_2	240	15.5	2.86	2.37×10^{10}	41

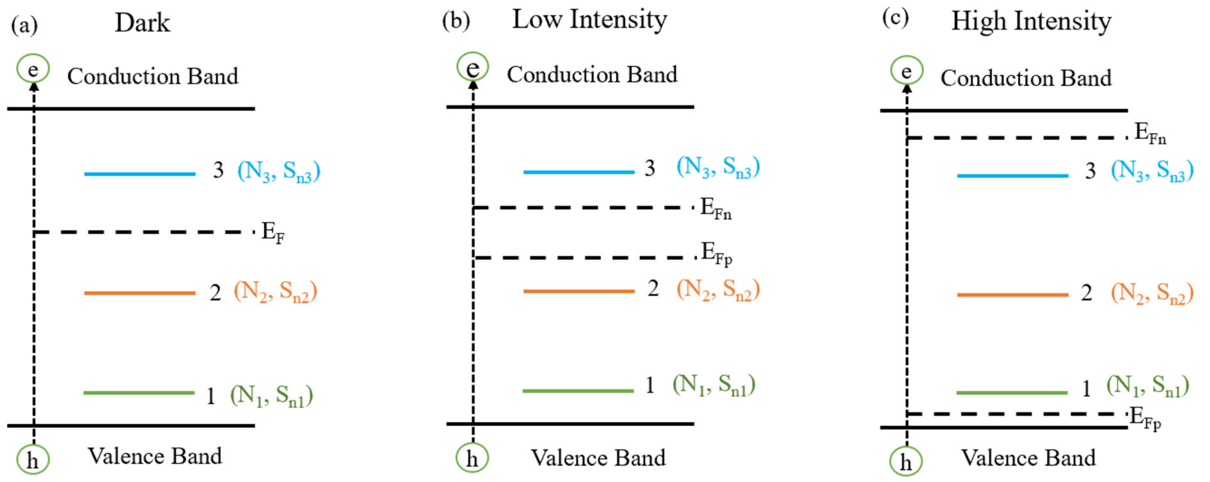

Fig. 9 Model to explain the origin of the superlinear behavior of the photocurrent. (a) Three different types of recombination centers (1–3) with different capture cross-sections and densities, along with the position of the Fermi level in the dark. The variation of the quasi-Fermi level in low intensity and high intensity of light is shown in (b) and (c) respectively.

originally proposed by Rose *et al.*,[43] as illustrated in Fig. 9. For simplicity, we consider three types of recombination centers (RCs), each characterized by distinct energy levels (N_i) and electron capture cross-sections (S_{ni}). As previously mentioned, RCs can originate from in-gap defect states, typically associated with selenium vacancies or other structural imperfections.

In the present model, type-1 centers (density N_1) are located near the valence band, characterized by a large hole capture cross-section ($S_{\mathrm{h}1}$) and a small electron capture cross-section ($S_{\mathrm{e}1}$). The type-2 and type-3 centers (density N_2 and N_3) are located near the mid-gap and close to the conduction band, respectively, and possess high capture cross-sections for both electrons and holes. Under dark conditions, the Fermi level (E_F) lies above centers 1 and 2 and below center 3. Upon illumination, the concentrations of photogenerated electrons and holes increase, shifting the quasi-Fermi levels, as shown in Fig. 9(b). At sufficiently high light intensities, type-3 centers, which are initially empty, begin to fill with electrons. This reduces the overall recombination rate, leading to the onset of superlinear photocurrent behavior. The nature of this behavior is further determined by the relative capture cross-sections and density of states of the recombination centers such that, if $S_{\mathrm{e}1} \approx S_{\mathrm{e}2} \approx S_{\mathrm{e}3}$ and $N_1 \approx N_2 \approx N_3$, the recombination rate increases steadily with increasing light intensity, potentially leading to linear or weakly superlinear behavior. In the second scenario, if $S_{\mathrm{e}1} \ll S_{\mathrm{e}2} \ll S_{\mathrm{e}3}$ and $N_1 \approx N_2 \approx N_3$, the recombination through centers 1 and 2 becomes inefficient, resulting in a sublinear photoresponse. However, if $S_{\mathrm{e}1} \ll S_{\mathrm{e}2} \ll S_{\mathrm{e}3}$ and $N_1 \gg N_2 \gg N_3$, the low density of states in center 3 causes it to saturate quickly at high light intensities, which reduces the overall recombination rate, resulting in strong superlinear behavior.

In the case of pristine $\mathrm{SnSe_2}$, a high density of Se vacancies results in $N_1 \gg N_2 \gg N_3$, favoring such superlinear photoresponse. Upon Fe doping, the introduction of Fe atoms modifies the defect landscape and increases the density of electronic states. As evident from the temperature-dependent resistance measurements, Fe-doping leads to a decrease in activation energy. This suggests that Fe-doping introduces donor-like defect states below the conduction band, thereby enhancing the density of states, particularly near center 3. This delays the saturation of recombination centers at high intensity, thus reducing the degree of superlinearity. This explains the observed decrease in the power-law exponent, γ, from 1.49 for pristine to 1.33 for Fe-doped $\mathrm{SnSe_2}$.

4 Conclusion

In summary, we have demonstrated that Fe doping in $\mathrm{SnSe_2}$ single crystals simultaneously modifies their electronic transport, vibrational dynamics, and magnetic ordering, while also giving rise to unusual photoconductive behavior. Temperature-dependent Raman spectroscopy revealed that lattice symmetry is preserved, yet phonon modes undergo measurable shifts consistent with enhanced anharmonicity and electron–phonon coupling. Electrical transport showed band-gap narrowing and reduced activation energy upon doping, while magnetic measurements uncovered the emergence of ferromagnetic interactions absent in pristine $\mathrm{SnSe_2}$. Photoconductivity studies further revealed a pronounced superlinear photocurrent response, which we explained through a trap-assisted recombination model involving dopant and defect-induced states.

Collectively, these findings establish Fe-doped $\mathrm{SnSe_2}$ as a model system for probing the coupled roles of charge, lattice, and spin degrees of freedom in van der Waals semiconductors. More broadly, they illustrate how transition-metal substitution can serve as a general strategy for engineering multifunctional behavior in layered materials, offering fundamental insights into the design of systems where optical, electronic, and magnetic responses are intrinsically intertwined.

Author contributions

Aarti Lakhara: conceptualization, analysis, investigation, data curation, methodology, writing – original draft, visualization, and software. P. A. Bhobe: conceptualization, methodology, project administration, supervision, and writing – review & editing.

Conflicts of interest

There are no conflicts to declare.

Data availability

The data supporting this article have been included in the main article and its supplementary information (SI). Supplementary information: energy dispersive X-ray spectroscopy (EDX) spectra and elemental mapping of $SnSe_2$ and Fe-doped $SnSe_2$ bulk single crystals, and UV-Vis measurement of polycrystalline samples. See DOI: https://doi.org/10.1039/d5cp03461b.

The data are also available from the authors upon request.

All data will be available through the repository maintained by the Central Library, IIT Indore, in due course of time.

Acknowledgements

Aarti Lakhara acknowledges DST-INSPIRE (File: DST/INSPIRE/03/2019/001146/IF190704), New Delhi, for providing the research fellowship. We also thank Professor Pratap Raychaudhuri and Ganesh Jangam from the Tata Institute of Fundamental Research, Mumbai, for their help in magnetic measurement.

References

1 A. Chaves, J. G. Azadani, H. Alsalman, D. Da Costa, R. Frisenda, A. Chaves, S. H. Song, Y. D. Kim, D. He and J. Zhou, *et al.*, *npj 2D Mater. Appl.*, 2020, **4**, 29.
2 C. S. Boland, Y. Sun and D. G. Papageorgiou, *Nano Lett.*, 2024, **24**, 12722–12732.
3 D. Kim, J. Pandey, J. Jeong, W. Cho, S. Lee, S. Cho and H. Yang, *Chem. Rev.*, 2023, **123**, 11230–11268.
4 S. Jin, Y. Liu, Z. Deng, T. Wang, S. Xu, Y. Chen, X. Jiang, C. Liang, J. Hong and S.-W. Cheong, *et al.*, *Adv. Mater.*, 2025, 2501935.
5 M. Zhong, C. Shen, L. Huang, H.-X. Deng, G. Shen, H. Zheng, Z. Wei and J. Li, *npj 2D Mater. Appl.*, 2019, **3**, 1.
6 C. Guo, Z. Tian, Y. Xiao, Q. Mi and J. Xue, *Appl. Phys. Lett.*, 2016, **109**, 203104.
7 T. Liang, C. Hu, M. Lou, Z. Feng, D. Wang, X. Cai and L. Lin, *Langmuir*, 2023, **39**, 10769–10778.
8 J. Xia, D. Zhu, L. Wang, B. Huang, X. Huang and X.-M. Meng, *Adv. Funct. Mater.*, 2015, **25**, 4255–4261.
9 P. Yu, X. Yu, W. Lu, H. Lin, L. Sun, K. Du, F. Liu, W. Fu, Q. Zeng and Z. Shen, *et al.*, *Adv. Funct. Mater.*, 2016, **26**, 137–145.
10 X. Zhou, L. Gan, W. Tian, Q. Zhang, S. Jin, H. Li, Y. Bando, D. Golberg and T. Zhai, *Adv. Mater.*, 2015, **27**, 8035–8041.
11 S. Weng, W. Zhen, X. Yan, Z. Yue, H. Hu, F. Xu, R. Zhang, L. Pi, W. Zhu and C. Zhang, *J. Phys.: Condens. Matter*, 2021, **33**, 395001.
12 S. Dong, X. Liu, X. Li, V. Kanzyuba, T. Yoo, S. Rouvimov, S. Vishwanath, H. G. Xing, D. Jena and M. Dobrowolska, *et al.*, *APL Mater.*, 2016, **4**, 032601.
13 H. Huang, A. Rahman, J. Wang, Y. Lu, R. Akiyama and S. Hasegawa, *J. Appl. Phys.*, 2021, **130**, 223903.
14 C. K. Zankat, P. Pataniya, G. Solanki, K. Patel, V. Pathak, N. Som and P. K. Jha, *Mater. Sci. Semicond. Process.*, 2018, **80**, 137–142.
15 M.-X. Zhai, X. Liang and D.-X. Li, *Results Phys.*, 2022, **39**, 105733.
16 H. A. Huy, D. K. Nguyen, R. Ponce-Pérez, J. Guerrero-Sanchez and D. Hoat, *Mater. Today Commun.*, 2023, **36**, 106511.
17 D. Hoat and J. Guerrero-Sanchez, *Mater. Adv.*, 2024, **5**, 1746–1755.
18 H. T. P. Thuy, V. V. On, J. Guerrero-Sanchez and D. Hoat, *Appl. Phys. A:Mater. Sci. Process.*, 2025, **131**, 219.
19 J. Rodríguez-Carvajal, *Phys. B*, 1993, **192**, 55.
20 A. Le Bail, H. Duroy and J. L. Fourquet, *Mater. Res. Bull.*, 1988, **23**, 447.
21 O. Agnihotri, A. Garg and H. Sehgal, *Solid State Commun.*, 1975, **17**, 1537–1540.
22 G. Lucovsky, J. Mikkelsen Jr, W. Liang, R. White and R. Martin, *Phys. Rev. B*, 1976, **14**, 1663.
23 A. Taube, A. Łapińska, J. Judek and M. Zdrojek, *Appl. Phys. Lett.*, 2015, **107**, 013105.
24 W. Zhou, Z. Yu, H. Song, R. Fang, Z. Wu, L. Li, Z. Ni, W. Ren, L. Wang and S. Ruan, *Phys. Rev. B*, 2017, **96**, 035401.
25 M. Balkanski, R. Wallis and E. Haro, *Phys. Rev. B:Condens. Matter Mater. Phys.*, 1983, **28**, 1928.
26 S. M. Stishov, A. E. Petrova, V. A. Sidorov and D. Menzel, *Phys. Rev. B:Condens. Matter Mater. Phys.*, 2012, **86**, 064433.
27 S. Wu, Z. Xu, S. C. Haley, S. F. Weber, A. Acharya, E. Maniv, Y. Qiu, A. Aczel, N. S. Settineri and J. B. Neaton, *et al.*, *Phys. Rev. X*, 2022, **12**, 021003.
28 M. Ghalawat and P. Poddar, *J. Phys. Chem. C*, 2022, **126**, 4655–4663.
29 D. Duong, J. Xing, E. Thareja, S. Huang, S. Crittenden, W. A. Shelton and R. Jin, *Phys. Rev. B*, 2024, **109**, 224512.
30 B. Li, T. Xing, M. Zhong, L. Huang, N. Lei, J. Zhang, J. Li and Z. Wei, *Nat. Commun.*, 2017, **8**, 1958.
31 H. K. Singh, N. S. Singh, P. P. Mohapatra, P. K. Giri, S. S. Meena and P. Dobbidi, *Phys. Rev. B*, 2024, **110**, 235124.
32 C. Fan, Q. Yue, J. Yang, Z. Wei, S. Yang and J. Li, *Appl. Phys. Lett.*, 2014, **104**, 202105.
33 W. Zhang, J.-K. Huang, C.-H. Chen, Y.-H. Chang, Y.-J. Cheng and L.-J. Li, *Adv. Mater.*, 2013, **25**, 3456–3461.
34 T. V. Vu, V. H. Chu, J. Guerrero-Sanchez and D. Hoat, *ACS Appl. Electron. Mater.*, 2024, **6**, 3647–3656.
35 S. Nandi, K. Ghosh, M. Meyyappan and P. Giri, *ACS Appl. Electron. Mater.*, 2023, **5**, 6985–6995.
36 P. Hu, L. Wang, M. Yoon, J. Zhang, W. Feng, X. Wang, Z. Wen, J. C. Idrobo, Y. Miyamoto and D. B. Geohegan, *et al.*, *Nano Lett.*, 2013, **13**, 1649–1654.

37 V. K. Sangwan, D. G. Chica, T.-C. Chu, M. Cheng, M. A. Quintero, S. Hao, C. E. Mead, H. Choi, R. Zu and J. Sheoran, *et al.*, *Sci. Adv.*, 2024, **10**, eado8272.

38 B. Chitara, L. Panchakarla, S. Krupanidhi and C. Rao, *Adv. Mater.*, 2011, **23**, 5419–5424.

39 P. M. Pataniya, M. Tannarana, C. K. Zankat, S. A. Bhakhar, S. Narayan, G. K. Solanki, K. D. Patel, P. K. Jha and V. M. Pathak, *J. Phys. Chem. C*, 2020, **124**, 2251–2257.

40 C. Fan, Z. Liu, S. Yuan, X. Meng, X. An, Y. Jing, C. Sun, Y. Zhang, Z. Zhang and M. Wang, *et al.*, *ACS Appl. Mater. Interfaces*, 2021, **13**, 35889–35896.

41 A. J. Khimani, S. H. Chaki, M. Deshpande, S. M. Chauhan and J. P. Tailor, *Mater. Lett.*, 2019, **236**, 187–189.

42 C. Xie, C. Mak, X. Tao and F. Yan, *Adv. Funct. Mater.*, 2017, **27**, 1603886.

43 A. Rose, *Phys. Rev.*, 1955, **97**, 322.